Filtered Back-Projection in 4π Compton Imaging With a Single 3D Position Sensitive CdZnTe Detector

Dan Xu, *Student Member, IEEE*, and Zhong He, *Senior Member, IEEE*

Abstract—**The Compton scattering camera can provide higher detection efficiency since the use of a mechanical collimator is not required. Several image reconstruction algorithms for Compton scattering cameras, such as maximum likelihood method and ART, can provide good imaging performance but are indirect and computational intensive. A direct reconstruction algorithm, such as filtered back-projection, is preferable if computational time is critical. Parra proposed an analytical inversion algorithm from cone-beam projections for Compton scattering cameras with a complete data set. In reality, a Compton camera is always limited by its configuration and can only provide an incomplete data set with a finite range of scattering angles. In this paper, we investigate a filtered back-projection algorithm applied to single 3-dimensional position sensitive CdZnTe detectors.**

Index Terms—**3-dimensional position sensitive CdZnTe detector, compton imaging, filtered back-projection.**

I. INTRODUCTION

A COMPTON-SCATTERING gamma camera records two or more interactions of each incident photon within the detector. The scattering angle can be deduced from energy depositions at each interaction position, and the direction of the incident photon is restricted on a cone with its vertex placed on the first scattering location. Unlike Anger cameras used in SPECT, this imaging technique does not require a mechanical collimator, and therefore is sometimes referred to as electronic collimation [1]. A Compton scattering camera usually holds the promise of a much higher efficiency than Anger cameras due to the elimination of the mechanical collimator, thus better counting statistics. However, since the direction of each incident photon can only be back projected onto a cone, there is less information provided by each event compared to mechanical collimation. Furthermore, the lack of a collimator complicates the reconstruction algorithm since the angular uncertainty now is related to energy resolution as well as position resolution, and can vary from event tevent.

Various reconstruction algorithms have been proposed since the introduction of Compton cameras [2], most of which are iterative algorithms [3], [4] since direct reconstruction is more difficult to implement in Compton imaging than traditional computed tomography, in which filter back-projection has found great success. However, the iterative algorithms are usually computationally intensive and their convergence points are often ambiguous. Therefore it is necessary to explore the possibility of applying direct reconstruction algorithms for Compton imaging.

Cree and Bones [5] have developed a direct reconstruction algorithm by severely limiting the scattering direction to be perpendicular to the detector array. Basko *et al.*.[6] established an analytical inversion method from cone surface projections using spherical harmonics without considering the distribution of possible scattering angles. Parra [7] developed an analytical inversion algorithm for the complete data set of all possible scattering angles based on the Klein-Nishina formula. In practice, as Tomitani and Hirasawa [8] pointed out, an actual Compton camera is almost impossible to provide a data set with a full range of scattering angles due to the limitation in the configuration of the detector system, and the difficulty in detecting small-angle scattering events. Tomitani further proposed an algorithm for limited angle Compton camera data set. However, in an actual Compton camera system, the detection efficiency varies at different scattering angles. This is partly due to the variation of path length of the detection material at different scattering directions, and partly due to the change of energy of scattered photons at different scattering angles. Therefore, the measured distribution of scattering angle will be different from that of the Klein-Nishina formula. In our case, simulations were performed to provide the point spread function (PSF) of the system. This accounts for the influence of the detector geometry on the distribution of scattering angles. Furthermore, a simpler analytical approach to the point spread function for limited angle Compton camera is proposed in this paper, and the result is compared with the point spread function obtained by simulations.

Three-dimensional position sensitive CdZnTe detector is a novel device in Compton imaging. The detector used in this work is 15 mm × 15 mm × 10 mm in dimension and employs an 11×11 pixel anode array on one 15×15 mm^2 surface. The depth of interaction is obtained by measuring the electron drifting times from the interaction positions to the collecting anodes. On this device, the position resolution is about 1.2 mm in each direction, and energy resolutions are 1.1% FWHM for single pixel events and 1.6% FWHM for two pixel events at 662 keV [9]. Since virtually each point within the detector volume can act as both the scattering detector and the absorption detector as on a conventional two layer Compton imager, the efficiency of this device is much higher than traditional two detector systems given the same total detection volume. Since the order of gamma-ray interactions cannot be obtained from time-of-flight measurement due to the poor timing resolution on CdZnTe and the small separation distance between

Manuscript received October 29, 2004; revised May 26, 2006. This work was supported in part by the U.S. Department of Energy/NNSA Na-22 Office under Grant DE-FG03-01NN20122.

The authors are with the Nuclear Engineering and Radiological Sciences Department, University of Michigan, Ann Arbor, MI 48109 USA (e-mail: xud@engin.umich.edu).

Digital Object Identifier 10.1109/TNS.2006.880974

scattering positions, sequence reconstruction must be applied based on energy depositions. Various sequence reconstruction algorithms have been examined and good results have been achieved [10], [11].

Since the size of a single detector is small, the ability to perform 3D source imaging is limited to the vicinity of the device. When the source is far away from the detector, the imaging can be approximated by shifting the first interaction position to the center of the detector. In this case, the cone-beam is projected onto a unit sphere and forms a ring. Thanks to the recent development in fast Fourier transform algorithms on the 4π-sphere [12]–[14], the transform from a 4π-sphere image into spherical harmonics is no longer a computational barrier. As a result, the reconstruction algorithm discussed in this paper is based on the cone-beam projection on the unit sphere.

II. IMAGE GENERATION

For simplicity, we first assume that the detector system has perfect position and energy resolutions, large enough size so that no secondary scattered photon can escape, and the ability to provide correct interaction sequences. We also assume that enough counts are collected so that any artifact caused by statistics is ignored. For a given source distribution $g(\vec{\Omega})$, the summation image $g'(\vec{\Omega}')$ of the cone-beam projections obtained by the measurement is a convolution of the source distribution $g(\vec{\Omega})$ with the point spread function, which is the summation image of a point like source. Since the point spread function is azimuthal symmetric, we can write it as $h(\cos\omega)$.

$$g'(\vec{\Omega}') = \int_{S^2} d\vec{\Omega} g(\vec{\Omega}) h(\cos\omega) \tag{1}$$

in which ω is the angle between $\vec{\Omega}$ and $\vec{\Omega}'$.

Considering an arbitrary function $f(\vec{\Omega})$ defined on the 4π-sphere, it can be expanded in the spherical harmonics domain by the following transform equations:

$$f(\vec{\Omega}) = \sum_{l=0}^{+\infty} \sum_{m=-l}^{m=l} F_l^m Y_l^m(\vec{\Omega}) \tag{2}$$

in which, the spherical harmonics coefficients F_l^m can be calculated by:

$$F_l^m = \int_{S^2} d\vec{\Omega} f(\vec{\Omega}) Y_l^{m*}(\vec{\Omega}). \tag{3}$$

Here, $Y_l^m(\vec{\Omega})$ are the spherical harmonics on 4π-sphere space S^2 and $Y_l^{m*}(\vec{\Omega})$ are the complex conjugate of the spherical harmonics:

$$Y_l^m(\theta,\varphi) = \sqrt{\frac{(2l+1)}{4\pi} \cdot \frac{(l-m)!}{(l+m)!}} P_l^m(\cos\theta) e^{im\phi} \tag{4}$$

in which $P_l^m(\cos\theta)$ are the associated Legendre polynomials.

According to the spherical convolution theorem [14], we can get from (1): s

$$G_l'^m = \sqrt{\frac{4\pi}{2l+1}} G_l^m H_l^0 \tag{5}$$

where $G_l'^m$, G_l^m and H_l^0 are the transformations of $g'(\vec{\Omega}')$, $g(\vec{\Omega})$ and $h(\cos\omega)$ in the spherical harmonics domain, respectively.

From (3),

$$\begin{aligned} H_l^0 &= \int_{S^2} d\vec{\Omega} h(\cos\omega) Y_l^{0*}(\vec{\Omega}) \\ &= \int_{S^2} d\vec{\Omega} h(\cos\omega) \sqrt{\frac{2l+1}{4\pi}} P_l^0(\cos\omega) \\ &= \sqrt{\pi(2l+1)} \int d(\cos\omega) h(\cos\omega) P_l^0(\cos\omega). \end{aligned} \tag{6}$$

For a function defined on $[-1,1]$ such as $h(\cos\omega)$, it can also be expanded into the sum of the Legendre polynomials:

$$h(\cos\omega) = \sum_{l=0}^{+\infty} H_l P_l(\cos\omega). \tag{7}$$

The coefficients are defined by:

$$H_l = \frac{2l+1}{2} \int d(\cos\omega) h(\cos\omega) P_l(\cos\omega). \tag{8}$$

By comparing (6) and (8), we find:

$$H_l^0 = \sqrt{\frac{4\pi}{2l+1}} H_l. \tag{9}$$

After replacing H_l^0 with (9) in (5), the following equation is derived:

$$G_l^m = \frac{(2l+1) G_l'^m}{4\pi H_l}. \tag{10}$$

So, to deconvolve the point spread function $h(\cos\omega)$ from the summation image of cone-beam projections $g'(\vec{\Omega}')$, we need to first transform the summation image into spherical harmonics domain to obtain $G_l'^m$, then by (10), the spherical harmonics coefficients of the source image G_l^m can be computed. The source image $g(\vec{\Omega})$ is obtained by the inverse transformation of the coefficients G_l^m into the 4π-sphere space. This is analogous to the deconvolution procedure in Cartesian coordinates.

Comparing (10) with (1) and (5), the following deconvolution formula is obtained:

$$g(\vec{\Omega}) = \int_{S^2} d\vec{\Omega}' g'(\vec{\Omega}') \tilde{h}(\cos\omega) \tag{11}$$

in which $\tilde{h}(\cos\omega)$ is a function with Legendre polynomial coefficients:

$$\tilde{H}_l = \left(\frac{2l+1}{4\pi}\right)^2 \cdot \frac{1}{H_l}. \tag{12}$$

The summation image $g'(\vec{\Omega}')$ is the sum of many cone-beam projections from individual events, as we do the reconstruction

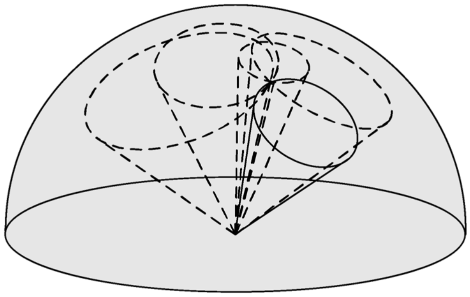

Fig. 1. Summation of cone-beam projections on the unit sphere.

in list mode (Fig. 1). For a specific event i, the projection of the cone beam on the unit sphere is a ring defined by cone axis direction $\vec{\Omega}_i$, and cone half angle ω_i. This ring is the projection image $g'_i(\vec{\Omega'})$ of event i.

$$g'(\vec{\Omega'}) = \sum_{i=1}^{N} g'_i(\vec{\Omega'}). \tag{13}$$

According to the linear property of the spherical convolutin, (11) can be rewritten as:

$$g(\vec{\Omega}) = \sum_{i=1}^{N} \int_{S^2} d\Omega' g'_i(\vec{\Omega'}) \tilde{h}(\cos\omega) \tag{14}$$

which means the filtering can be done event-by-event, which makes real-time imaging possible. The price is the requirement of doing Fourier transform on the 4π-sphere for each event. However, the spherical convolution is rotation invariant, and $g'_i(\vec{\Omega'})$ is a function which is azimuthal symmetric around the cone axis $\vec{\Omega}_i$, which means that only Legendre polynomial expansion is needed. With the help of fast Fourier transform algorithms on the 4π-sphere developed in recent years, the computational cost is minimized.

III. POINT SPREAD FUNCTION

The point spread function is determined by the fundamental principles of Compton scattering cameras. Without considering the detector noise, the summation image of the many cone-beam projections from a point-like source is a distributed image rather than a delta function at the source direction. This is due to the fact that the source direction information provided by each event is distributed on a cone. Fig. 2 shows the contribution of a cone back-projection to the point spread function.

Parra gave the point spread function of a Compton camera from simple back projection based on an assumption that each point on all back projection rings has the same value [7]. Here we give another simpler approach to calculate the point spread function.

Suppose a mono-energetic source irradiates an idealized detector from above. When the detector detects an event with scatter angle θ, the cone-beam projection will generate a ring with half angle θ on the unit 4π-sphere. Since the detector is perfect, the reconstructed cone should always pass the true source location, which is at the zenith of the unit sphere. When many rings are reconstructed on the sphere, the back projection summation image is formed, which is also the point spread function of the Compton camera. Since the system is symmetric around z axis, the point spread function thus is only related to the polar angle ω. Therefore, the point spread function is also written as a function of a single variable, $h(\cos\omega)$.

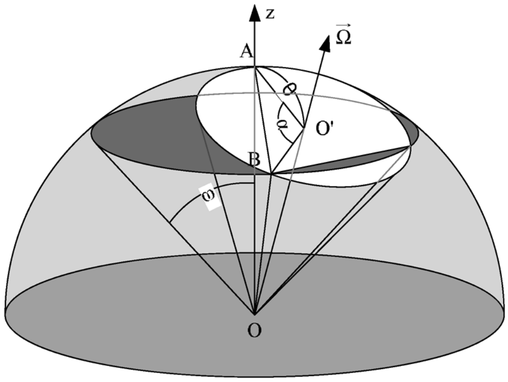

Fig. 2. The contribution of a cone-beam projection with cone axis $\vec{\Omega}$ and half angle ω to the PSF.

The values assigned to different pixels on the projection ring should be uniform, since the gamma ray could come from any direction on that ring, provided that there is no polarization information obtained. If we assume that each event carries the same amount of information, the sum of the values on each back projection ring should be normalized. Since the perimeter of each ring is proportional to $\sin\theta$, the values on each back projection cone should be proportional to $1/\sin\theta$. If a back projection ring with half angle θ intersects a ring on the unit sphere with half angle ω at angle α as shown in Fig. 2, the contribution of this ring to the point spread function from ω to $\omega + d\omega$ is proportional to $d\alpha/\sin\theta$. Therefore, the sum of the point spread function between ω and $\omega + d\omega$ is proportional to the integral of all possible scattering angles:

$$h(\cos\omega)\sin\omega d\omega = \int_0^{\pi} d\theta K(\theta) \sin\theta \frac{d\alpha}{\sin\theta} \tag{15}$$

in which $K(\theta)$ is the Klein-Nishina cross section formula and $K(\theta)\sin\theta$ is proportional to the probability density function of scattering angle θ, as shown in (16) at the bottom of the page, in which r_0 is the classical electron radius, and $\gamma = E_0/m_e c^2$ is the ratio of the initial gamma ray and rest mass energy of an electron.

As a result, the contribution of cone-beam projections to the point spread function at angle ω can be evaluated by:

$$h(\cos\omega) = \int_0^{\pi} d\theta K(\theta) \frac{1}{\sin\omega} \cdot \frac{d\alpha}{d\omega}. \tag{17}$$

$$K(\theta) = \frac{r_0^2}{2} \frac{(1+\cos^2\theta)[1+\gamma(1-\cos\theta)] + \gamma^2(1-\cos\theta)^2}{[1+\gamma(1-\cos\theta)]^3} \tag{16}$$

In triangle $ABO', |AB| = 2\sin(\omega/2)$, and $|O'A| = |O'B| = \sin\theta$. The law of cosine gives:

$$|AB|^2 = |O'A|^2 + |O'B|^2 - 2|O'A||O'B|\cos\alpha. \tag{18}$$

Therefore, the following geometrical relationship is obtained:

$$\cos\alpha = 1 - \frac{2\sin^2\frac{\omega}{2}}{\sin^2\theta} \tag{19}$$

As a result, (17) becomes:

$$h(\cos\omega) = \int_0^{\pi} d\theta K(\theta) \frac{1}{\sin\omega} \cdot \frac{\cos\frac{\omega}{2}}{\sqrt{\cos^2\frac{\omega}{2} - \cos^2\theta}}. \tag{20}$$

We notice when the scatter angle θ is smaller than $\omega/2$ or greater than $\pi - \omega/2$, the back projection cone will not contribute to the point spread function at ω, and the integral in (20) can be rewritten as:

$$h(\cos\omega) = \frac{1}{2\sin\frac{\omega}{2}} \int_{\omega/2}^{\pi-\omega/2} \frac{d\theta K(\theta)}{\sqrt{\cos^2\frac{\omega}{2} - \cos^2\theta}}. \tag{21}$$

This result differs from Parra's result with a term of $\sin\theta$ because of the assumption that each back projection ring contains the same amount of information.

Tomitani pointed out that in real Compton camera, the distribution of the scattering angle is always limited [8]. In our 3D position sensitive CdZnTe detector, this is especially true because of the sequence reconstruction algorithm. For events with scattering angle between η_1 and $\eta_2 (\eta_1 < \eta_2)$, the point spread function can be obtained by replacing $K(\theta)$ with $K'(\theta)$ in (21), in which $K'(\theta)$ is defined as:

$$K'(\theta) = \begin{cases} K(\theta) & \theta \in (\eta_1, \eta_2) \\ 0 & \text{otherwise} \end{cases}. \tag{22}$$

In this case, the point spread function is a complicated integral and needs to be solved numerically. For a specific situation in a 3D position-sensitive CdZnTe detector, the point spread function for incident photons with energy greater than $m_e c^2/2$ can be derived analytically (see Appendix), as shown in (23) at the bottom of the page, in which $f(\theta), \omega_1, \omega_2, K'(\theta)$ and $K''(\theta)$ are defined as:

$$f(\theta) = \frac{2}{\gamma^2(1-\cos\theta)} - \frac{1}{\gamma^4(1-\cos\theta)^2} \tag{24}$$

$$\cos\omega_1 = 1 - \frac{(m_e c^2)^2}{2E_0^2} \tag{25}$$

$$\cos\omega_2 = 1 - \frac{m_e c^2}{E_0} \tag{26}$$

$$K'(\theta) = \begin{cases} K(\theta) & \theta \in (0, \omega_1) \cup (\omega_2, \pi) \\ 0 & \text{otherwise} \end{cases} \tag{27}$$

$$K''(\theta) = \begin{cases} K(\theta) & \theta \in (\omega_1, \omega_2) \\ 0 & \text{otherwise} \end{cases}. \tag{28}$$

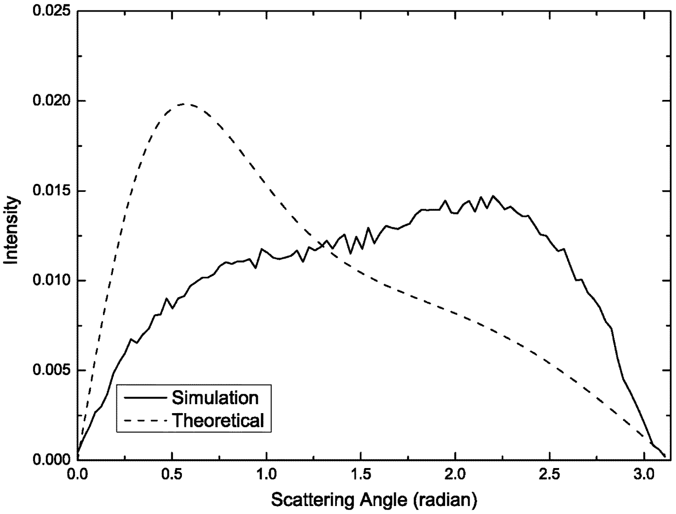

Fig. 3. The simulation shows that the actual scattering angle distribution of 662 keV gamma rays in our 3D CdZnTe detector is different from the theoretical prediction based on Klein-Nishina formula, thus the actual PSF should be different from (23).

However, the measured distribution of scattering angle on a real detector does not follow the Klein-Nishina formula because in a detector with limited size, not all Compton scattering events will be recorded. The detection efficiency varies for events with different scattering angles. For example, scattered photons at smaller scattering angles have higher energy than photons scattered at large angles, thus they are more likely to escape the detector. In another word, the actual scattering angle distribution favors large scattering angles comparing with the theoretical prediction of the Klein-Nishina formula. Fig. 3 shows the difference of scattering angle distributions between the prediction by the Klein-Nishina formula and our simulation on the 3D CdZnTe detector using Geant4 simulation package [15].

Therefore, the theoretical prediction of the point spread function using the Klein-Nishina formula cannot be applied directly on an actual Compton camera. Monte Carlo simulations using Geant4 packages were performed to provide the point spread function of a 15 mm× 15 mm× 10 mm 3D CdZnTe detector. In our simulations, charge sharing problem between neighboring pixel anodes caused by the finite initial electron cloud size and the diffusion of electrons were not modeled. The detector was idealized with perfect depth and energy resolution. The anode of the detector was still divided into an 11×11 pixel array to account for the pixellation effect. A 662 keV gamma ray source was placed 20cm away from the side of the detector, and only two-pixel full energy deposition events were recorded. Those two pixel events with correct sequences were reconstructed using simple back-projection to generate the point spread function image. The information carried by each event was set to be

---

$$h(\cos\omega) = \frac{1}{2\sin\frac{\omega}{2}} \int_{\omega/2}^{\pi-\omega/2} \frac{d\theta K'(\theta)}{\sqrt{\cos^2\frac{\omega}{2} - \cos^2\theta}} + \int_{\omega_1}^{\omega_2} \frac{2K''(\theta)d\theta}{\sqrt{4\sin^2\theta f(\theta) - \left[\sin^2\theta + f(\theta) - 4\sin^2\frac{\omega}{2}\right]^2}} \tag{23}$$

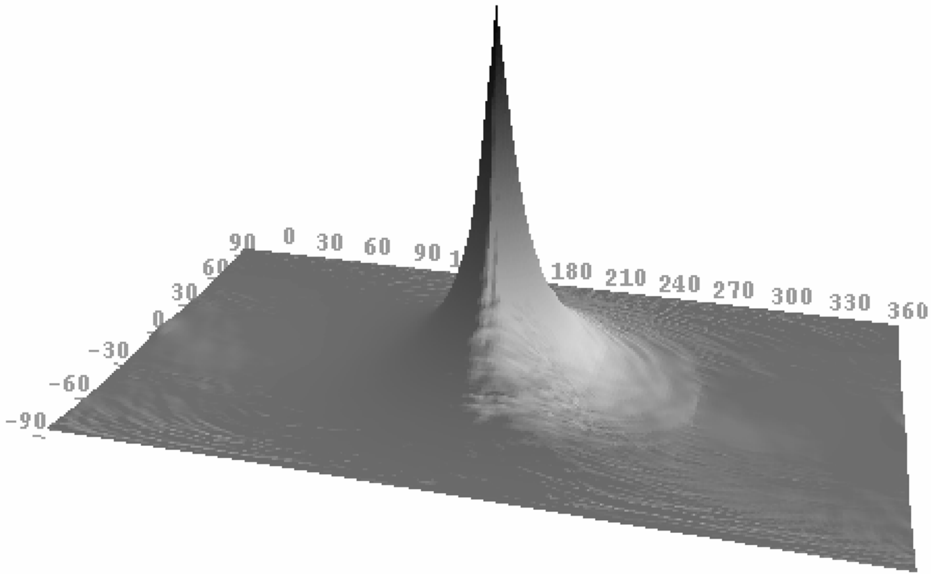

Fig. 4. Simulated PSF. A 662 keV gamma ray source was placed at the side of the detector, and only two-pixel full energy deposition events were reconstructed.

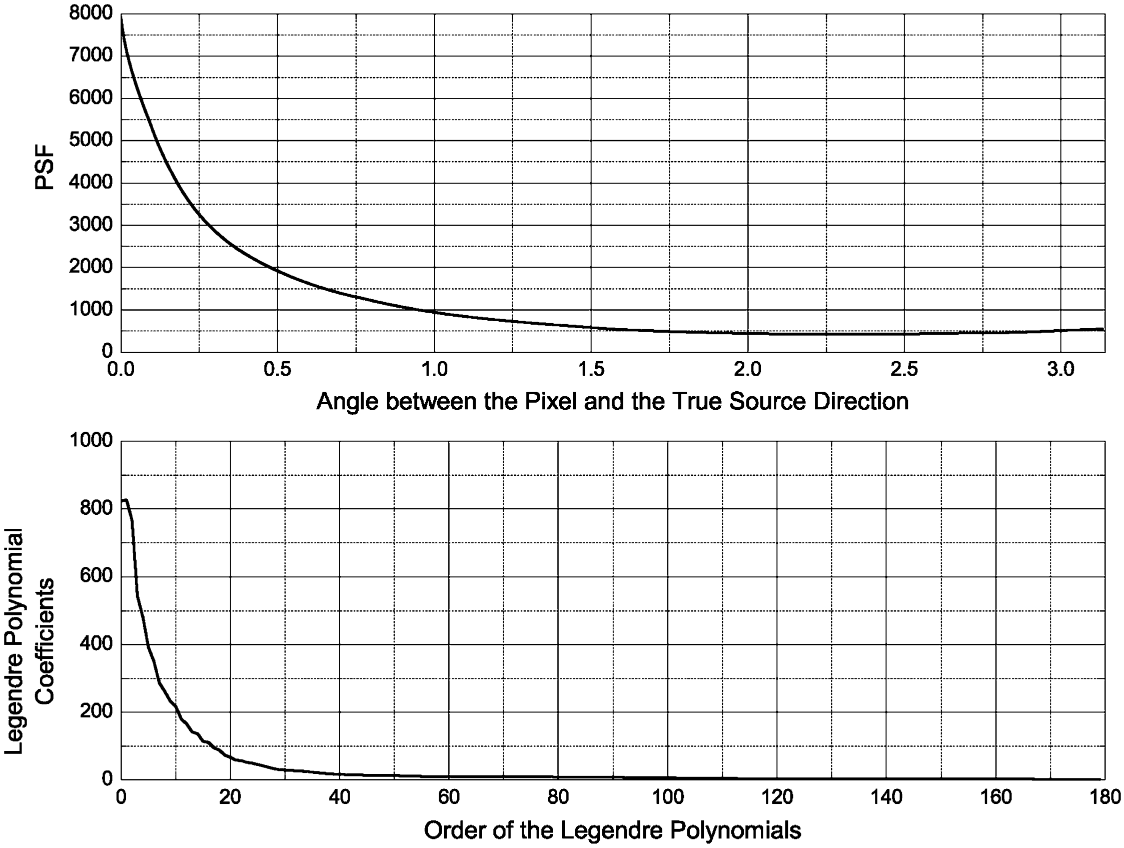

Fig. 5. The upper figure shows the simulated PSF of a 3D CdZnTe detector at 662 keV. Due to the azimuthal symmetry of the PSF, the Fourier transform of the PSF into the spherical harmonics domain only has Legendre polynomials. The coefficients of those Legendre polynomials are shown in the bottom figure.

the same, i.e., the contribution of each event to the summation image was normalized. The reconstructed point spread function from the simulated data is shown in Fig. 4.

When calculating the PSF from simulated data, it is desired to get the PSF as close as the true PSF of the system. Factors that can affect the PSF include scattering angle distribution, Doppler broadening, detector position and energy uncertainties, and sequence reconstruction. In the calculated PSF of Fig. 5, only scattering angle distribution, Doppler broadening, and detector pixellation were included. Because the energy and

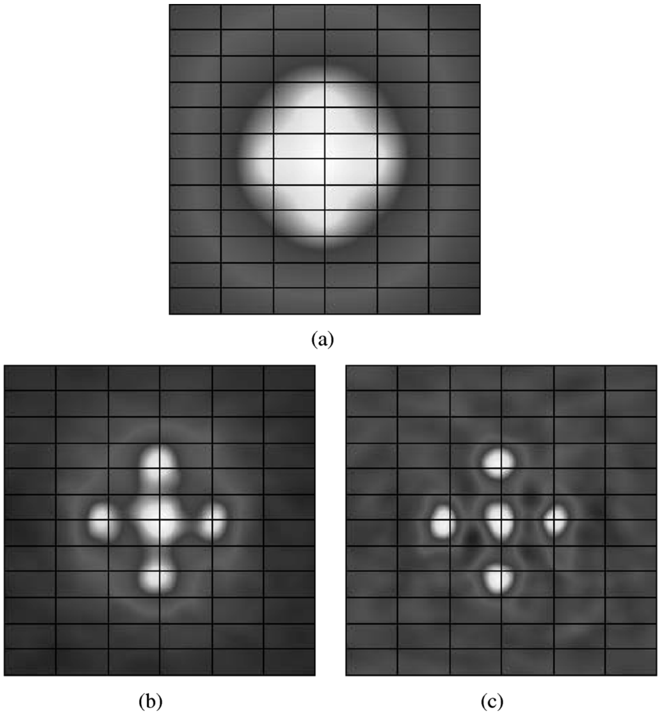
(a)

(b) (c)

Fig. 6. Reconstructed images of simulated data for five Cs-137 point sources. (a). Simple back-projection. The five sources can not be distinguished. (b). Filtered back-projection with the theoretical PSF using (23). The five sources can be distinguished. (c). Filter back-projection with the simulated PSF shown in Fig. 4. It has better angular resolution than the image reconstructed with the theoretical PSF.

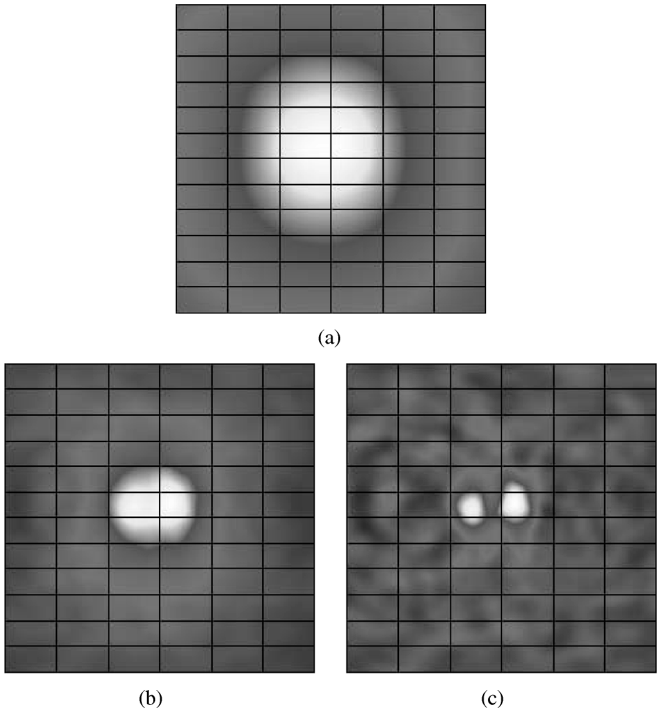
(a)

(b) (c)

Fig. 7. Reconstructed images of measured data from two Cs-137 sources separated by 15 degrees. (a). Simple back-projection of the reconstruction cones. The two sources can not be distinguished. (b). Filtered back-projection with the theoretical PSF using (23). The two sources can barely be distinguished. (c). Filtered back-projection with the simulated PSF shown in Fig. 4. The two sources can be distinguished clearly.

depth resolutions can vary from detector to detector, and different sequence reconstruction algorithms might be developed and applied, other factors were not included.

IV. RESULTS

The filtered back-projection algorithm described in previous sections has been applied to both simulations and measurements. In the simulations, five 662 keV points sources were placed in a cross shape at the side of the detector. The distances between the center source and four corner sources were 10 cm, and the distance between the center source and the detector was 25 cm. The detector was set to have a 5 keV FWHM electronic noise, an average ionization energy of 5 eV for each electron-hole pair, and a depth resolution of 1 mm FWHM. The point spread functions from both theoretical calculation using (23) and simulation were used to reconstruct the images. Low pass filtering is not needed for the theoretical point spread function since it does not vanish at high orders. However, as shown in Fig. 5, for the simulated point spread function, the coefficients of the Legendre polynomials vanish quickly as the order increases. To avoid instability problem in the filtered back-projection reconstruction, a low pass filter is usually adapted. However, a low pass filter with bandwidth D will limit the angular resolution to π/D. Therefore, if the bandwidth is too low, the system cannot achieve good angular resolution. In our algorithm, coefficients for orders greater than 15 were set to be constant which equals the value at the order of 15. This way, the system can achieve better angular resolution and avoid the instability problem. Fig. 6 shows the reconstructed image of the simulated data with simple back-projection, filtered back-projection with theoretical point spread function, and filtered back-projection with simulated point spread function, respectively.

This algorithm was also applied to the actual measurement. Two 10 μCi Cs-137 sources were placed 15 degrees apart and 10 cm away from one side of the detector. Only two-pixel events with full energy deposition were used to reconstruct the image. Neighboring pixel events with depth separation less than 2 mm were excluded since most of those events were charge sharing events. About 40 k good events were used in the reconstruction. The images reconstructed from the measured data are shown in Fig. 7. From Figs. 6 and 7 we can see that the filtered back-projection algorithm with the simulated point spread function has better angular resolution in the reconstructed image from both simulated and measured data. This indicates that the simulated PSF represents the actual PSF better than the theoretical PSF obtained from (23).

V. CONCLUSION

Filtered back-projection technique for Compton imaging reconstruction has been implemented on a real CdZnTe detector with 3D position sensing capability. The measured distribution of scattering angle differs from the prediction of the Klein-Nishina formula because of the detector geometry and variation of detection efficiency for photons scattered at different angles. As a result, the point spread function obtained by theoretical analysis based on the Klein-Nishina formula has limitations for practical Compton camera systems. In this

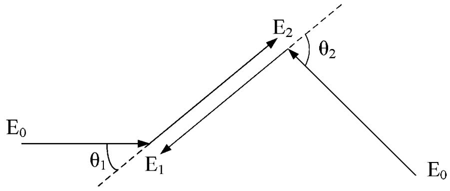

Fig. 8. Two possible sequences in a two-pixel event. θ_1 and θ_2 are the two possible scatter angles.

work, the theoretical PSF from the Klein-Nishina formula was derived, and the practical PSF for the 3D CdZnTe detector was obtained by Monte Carlo simulations. Both the theoretical and the simulated PSFs were used in our filtered back-projection reconstruction. The reconstructed image using the simulated PSF showed better angular resolution both for simulated and actual measured data. Currently, due to the limited size of our detector system, the PSF is very poor and limits the angular resolution of the filtered back-projection algorithm. Better detector system design with improved PSF will benefit the performance of the filtered back-projection algorithm in future Compton cameras.

In both the measurement and the simulation, the source is at 662 keV and placed at the side of the detector. The PSF was calculated based on the simulation result with this configuration. If the source is at different locations, the distribution of the scattering angle might be different, thus the PSF can be changed. However, since the asymmetry in the geometry is not significant for a 15 mm × 15 mm × 10 mm CdZnTe detector, the PSF of a point source at the side can still be applied to other source locations. For a detector configuration with large asymmetry, simulations should be performed to obtain the PSFs at different source locations. Different PSFs at different energies also need to be calculated from separate simulations, which could require a large amount of work. For each source location at each energy, the PSF can be discribed by a few coefficients of the Legendre polynomials. Therefore, it does not require a huge database to store a complete set of PSFs.

The filtered back-projection algorithm was performed in the spherical harmonic domain. With the recent advance in fast spherical harmonic transforms, the computational cost of the filtered back-projection algorithm was significantly reduced. Because of the linear property of the algorithm, the filtered back-projection reconstruction can be performed event-by-event, which enables the detector to perform real-time imaging.

APPENDIX

In our 3D position sensitive CdZnTe detector system, the sequence of interactions in a multiple pixel event must be reconstructed solely based on energy depositions. For simplicity, only the case of two-pixel events is considered in this paper. For those two pixel events, there are two possible interaction sequences and the sequence must be reconstructed before the back-projection (Fig. 8). The current sequence reconstruction algorithm performs the Compton edge test first. Those events with an energy deposition greater than the Compton edge of the incident gamma ray must deposit the smaller amount of energy first. For other events, although both sequences are possible, the interaction with higher energy deposition is chosen to be the first interaction since the possibility of these events is higher for incident photons with energy greater than 400 keV [16]. Other algorithms, such as deterministic algorithm by comparing the predicted probabilities of the two possible sequences, have been examined. Because of the small size of the detector, those algorithms show little advantage over the simple comparison algorithm.

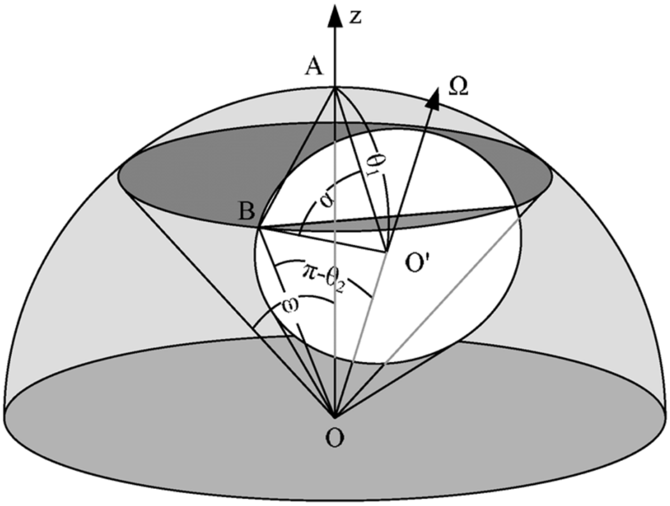

Fig. 9. The contribution of an incorrectly sequenced event to the PSF. The event generates a cone-beam projection with cone axis $\vec{\Omega}$ and half angle $\pi - \theta_2$

Two angles, ω_1 and ω_2, are defined in (25) and (26). From the definition, $0 < \omega_1 < \omega_2 < \pi$ when $E_0 > m_e c^2/2$. When the scattering angle is between 0 and ω_1, the energy deposition of the second interaction must be higher than the Compton edge. Since the reversed sequence is physically impossible, the sequence can always be reconstructed correctly. When the scattering angle is between ω_1 and ω_2, the first interaction deposits less energy than the second one, therefore the sequence is incorrectly determined by our algorithm. For these events, the reversed sequence is physically possible, and has higher probability if the incident direction of the gamma ray is unknown. Our algorithm selects the higher energy deposition as the first interaction. For events with scattering angle between ω_2 and π, the first interaction deposits more energy than the second one and their sequences are correctly reconstructed.

When the energy of the incident gamma ray is less than $m_e c^2/2, \cos\omega_1$ and $\cos\omega_2$ are less than -1. This means that the first interaction always deposits less energy than the second one and the sequence can be correctly reconstructed if the strategy of the sequence reconstruction algorithm is reversed for this energy range. So, our discussion here will only focus on scatterings with initial photon energy greater than $m_e c^2/2$.

Suppose the correct sequence is $E_1 \rightarrow E_2$, then we have:

$$\cos\theta_1 = 1 + \frac{m_0 c^2}{E_0} - \frac{m_0 c^2}{E_2} \tag{29}$$

$$\begin{aligned}\cos\theta_2 &= 1 + \frac{m_0 c^2}{E_0} - \frac{m_0 c^2}{E_1} \\ &= 1 + \frac{m_0 c^2}{E_0} - \frac{m_0 c^2}{E_0 - E_2}.\end{aligned} \tag{30}$$

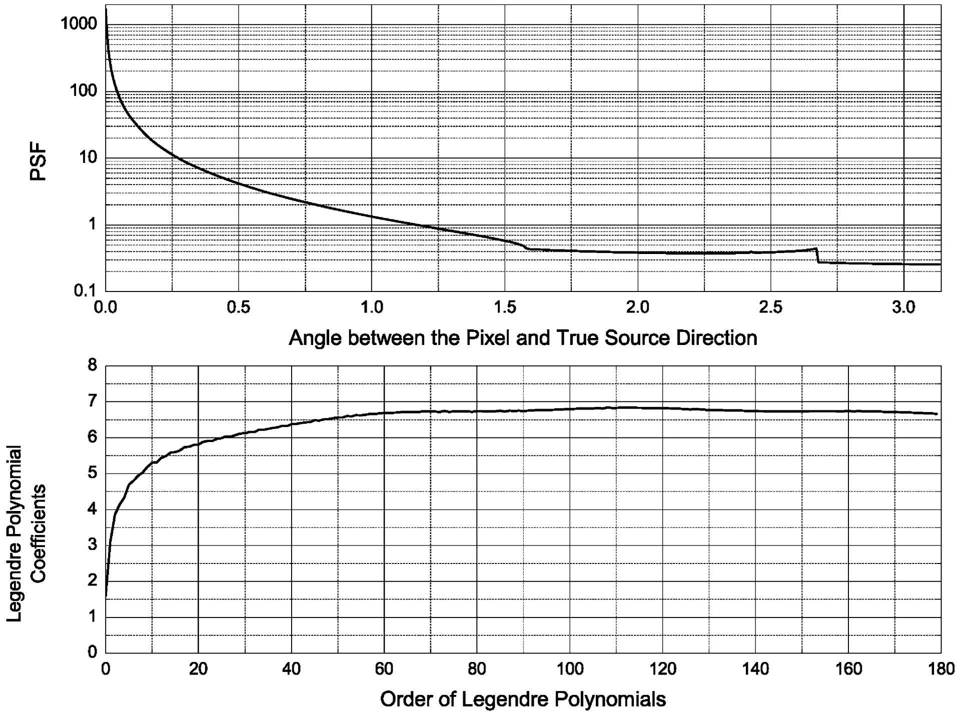

Fig. 10. The upper figure shows the PSF of all two-pixel events at 662 keV with sequence reconstruction algorithm applied. The bottom figure shows the Legendre polynomial coefficients when the PSF is Fourier transformed into spherical harmonics domain.

From (29) and (30) we get:

$$\cos\theta_2 = 1 - \frac{1}{\gamma^2(1-\cos\theta_1)}. \tag{31}$$

For events which can be correctly sequenced by our algorithm, i.e., events with scattering angle in region $[0, \omega_1]$ or $[\omega_2, \pi]$, their contribution to the point spread function $h_{\text{correct}}(\cos\omega)$ can be calculated by (21) and (22). Now we need to calculate the contribution of those incorrectly sequenced events to the point spread function.

The sequences corresponding to the two possible scatter angles are opposite, so when calculating the contribution of the incorrectly sequenced events to the point spread function, the angle between the cone and the E_2E_1 vector $\vec{\Omega}$ is $\pi - \theta_2$. The reconstructed cone based on an incorrectly sequenced event will not pass the true source position, unless $\theta_1 + \theta_2$ exactly equals to 180°. The contribution of an incorrectly sequenced event to the point spread function is shown in Fig. 9. As a result, (21) is not valid anymore. The PSF of the incorrectly sequenced events should be recalculated from (17).

In triangle $ABO', |AB| = 2\sin(\theta/2), |AO'| = \sin\theta_1$, and $|BO'| = \sin\theta_2$. By the law of cosine, the following geometry relationship is obtained:

$$\cos\alpha = \frac{\sin^2\theta_1 + \sin^2\theta_2 - 4\sin^2\frac{\omega}{2}}{2\sin\theta_1\sin\theta_2}. \tag{32}$$

As a result:

$$\frac{d\alpha}{d\omega} = \frac{2\sin\omega}{\sqrt{4\sin^2\theta_1\sin^2\theta_2 - \left(\sin^2\theta_1 + \sin^2\theta_2 - 4\sin^2\frac{\omega}{2}\right)^2}} \tag{33}$$

in which,

$$\sin^2\theta_2 = \frac{2}{\gamma^2(1-\cos\theta_1)} - \frac{1}{\gamma^4(1-\cos\theta_1)^2}.$$

Since θ_1 is the true scatter angle, $\theta_1 = \theta$. The contribution of those events with scattering angles between ω_1 and ω_2 to the point spread function is:

$$\begin{aligned} h_{\text{incorrect}}(\cos\omega) &= \int_{\omega_1}^{\omega_2} d\theta K(\theta)\frac{1}{\sin\omega}\cdot\frac{d\alpha}{d\omega} \\ &= \int_{\omega_1}^{\omega_2} \frac{2K''(\theta)d\theta}{\sqrt{4\sin^2\theta f(\theta) - \left[\sin^2\theta + f(\theta) - 4\sin^2\frac{\omega}{2}\right]^2}} \end{aligned} \tag{34}$$

where $f(\theta)$ is defined in (24).

The overall PSF for incident photons with energy greater than $m_ec^2/2$ now can be written as:

$$\begin{aligned} h(\cos\omega) &= h_{\text{correct}}(\cos\omega) + h_{\text{incorrect}}(\cos\omega) \\ &= \frac{1}{2\sin\frac{\omega}{2}}\int_{\omega/2}^{\pi-\omega/2} \frac{d\theta K'(\theta)}{\sqrt{\cos^2\frac{\omega}{2} - \cos^2\theta}} \\ &\quad + \int_{\omega_1}^{\omega_2} \frac{2K''(\theta)d\theta}{\sqrt{4\sin^2\theta f(\theta) - \left[\sin^2\theta + f(\theta) - 4\sin^2\frac{\omega}{2}\right]^2}} \end{aligned} \tag{35}$$

in which $\omega_1, \omega_2, K'(\theta)$ and $K''(\theta)$ are defined in (25), (26), (27) and (28), respectively.

The overall analytical point spread function at 662 keV and its Legendre polynomial coefficients of our 3D position sensitive CdZnTe detector are shown in Fig. 10. The scale in this figure differs from the scale in Fig. 5 because the PSF in this figure is calculated directly from (23) while the PSF in Fig. 5 is from the simple back-projection image, which depends on how many events are used in the reconstruction. By comparing the Legendre polynomial coefficients in Fig. 10 and Fig. 5 we can see that the PSF from the simulated data has much lower values for high-frequency components than the PSF from the theoretical calculation. This is because the pixellation of the detector blurs the simple back-projection image and suppresses the high-frequency components.

REFERENCES

[1] R. Brechner and M. Singh, “Iterative reconstruction of electronically collimated SPECT images,” *IEEE Trans. Nucl. Sci.*, vol. 37, no. 3, pp. 1328–1332, 1990.

[2] R. Todd, J. Nightingale, and D. Everett, “A proposed gamma camera,” *Nature*, vol. 251, pp. 132–134, 1974.

[3] M. Singh, “An electronically collimated gamma camera for single photon emission computed tomography. Part I: Theoretical considerations and design criteria,” *Med. Phys.*, vol. 10, no. 4, pp. 421–427, 1983.

[4] T. Hebert, R. Leahy, and M. Singh, “Three-dimensional maximum-likelihood reconstruction for an electronically collimated single-photon-emission imaging system,” *Opt. Soc. Amer.*, vol. 7, no. 7, pp. 1305–1313, 1990.

[5] M. J. Cree and P. J. Bones, “Towards direct reconstruction from a gamma camera based on compton scattering,” *IEEE Trans. Med. Imag.*, vol. 13, no. 2, pp. 398–407, 1994.

[6] R. Basko, G. L. Zeng, and G. T. Gullberg, “Application of spherical harmonics to image reconstruction for the compton camera,” *Phys. Med. Biol.*, vol. 43, no. 4, pp. 887–894, 1998.

[7] L. Parra, “Reconstruction of cone-beam projections from Compton scattered data,” *IEEE Trans. Nucl. Sci.*, vol. 47, no. 4, pp. 1543–1550, 2000.

[8] T. Tomitani and M. Hirasawa, “Image reconstruction from limited angle Compton camera data,” *Phys. Med. Biol.*, no. 12, pp. 2129–2145, 2002.

[9] F. Zhang, Z. He, D. Xu, G. Knoll, D. Wehe, and J. Berry, “Improved resolution for 3-D position sensitive CdZnTe spectrometers,” *IEEE Trans. Nucl. Sci.*, vol. 51, no. 5, pp. 2427–2431, 2004.

[10] C. E. Lehner, “4-Pi Compton Imaging Using a Single 3-D Position-Sensitive CdZnTe Detector,” Ph.D. thesis, Univ. Michigan, Ann Arbor, 2004.

[11] D. Xu, Z. He, C. E. Lehner, and F. Zhang, “4-pi Compton imaging with single 3D position sensitive CdZnTe detector,” in *Proc. SPIE*, 2004, vol. 5540, pp. 144–155.

[12] S. Kurds and D. Potts, “Fast spherical Fourier algorithms,” *Comput. Appl. Math.*, vol. 161, no. 1, pp. 75–98, 2003.

[13] D. M. Healy, J. D. N. Rockmore, P. J. Kostelec, and S. Moore, “FFTs for the 2-sphere-improvements and variations,” *Fourier Anal. Appl*, vol. 9, no. 4, pp. 341–385, 2003.

[14] J. R. Driscoll and D. M. Healy, “Computing fourier transforms and convolutions on the 2-Sphere,” *Adv. Appl. Math.*, vol. 15, no. 2, pp. 202–250, 1994.

[15] S. Agostinelli, J. Allison, K. Amako, J. Apostolakis, H. Araujo, P. Arce, M. Asai, D. Axen, S. Banerjee, and G. Barrand, “GEANT4-a simulation toolkit,” *Nucl. Instrum. Methods Phys. Res. A*, vol. 506, no. 3, pp. 250–303, 2003.

[16] C. Lehner, Z. He, and F. Zhang, “4-pi Compton imaging using a 3-D position-sensitive CdZnTe detector via weighted list-mode maximum likelihood,” *IEEE Trans. Nucl. Sci.*, vol. 51, no. 4, pp. 1618–1624, 2004.